Multi-scale (time and mass) dynamics of space objects
Proceedings IAU Symposium No. 364, 2022
A. Celletti, C. Galeş, C. Beaugé, A. Lemaitre, eds.
doi:10.1017/S1743921321001344

A cartographic study of spin-orbit coupling in binary asteroids

Mahdi Jafari Nadoushan

K. N. Toosi University of Technology, Tehran, Iran

Abstract. In the spin-orbit resonances, we assume that the orbit of the secondary asteroid around the primary is invariant, which is a reasonable assumption at first glance. Owing to the irregularity of asteroids' geometry and their effect on the mutual orbit, this assumption should be revised. Therefore, we focus on a binary asteroid with a spherical primary and a secondary with an irregular shape. When the shape of a secondary asteroid is not a sphere, the gravitational interaction is important, and we should consider the interaction of orbit and spin. We generate fast Lyapunov indicator (FLI) maps for both spin-orbit resonance and spin-orbit coupling problems and investigate the effect of orbit alternation on the structure of phase space.

Keywords. celestial mechanics, methods: numerical, minor planets, asteroids

1. Introduction

A spin-orbit resonance is a situation where the rotation period of a secondary asteroid and its motion around a primary asteroid are commensurate. When we consider a fixed orbit for the secondary and study its spin, we call the problem spin-orbit resonance (SOR). While, when we investigate the simultaneous alternation of orbit and spin of the secondary due to perturbations, we call it spin-orbit coupling (SOC). In the seminal work, Goldreich and Peale (1966) have formulated SOR in fixed eccentric orbits for planets and satellites. Wisdom *et al.* (1984) have studied chaotic motion in the spin-orbit problem through resonance overlapping criterion. Celletti and Chierchia (2000) have considered a nearly-integrable Hamiltonian model describing the conservative spin-orbit interaction. Nadoushan and Assadian (2016) have studied the overlap of the first- and second-order spin-orbit resonances for different values of system parameters. Misquero and Ortega (2020) have analytically investigated a dissipative spin-orbit problem and studied capturing into the synchronous resonance. In most previous works, it was assumed that the mutual orbit is invariable. Some recent works have considered a variable mutual orbit. Naidu and Margot (2015) have considered coupled spin and orbital motions of binary asteroids and showed the existence of a chaotic motion. Hou and Xin (2017) have analytically studied spin-orbit problem with a variable orbit and showed that the resonance center changes for some values of the system parameters. Wang and Hou (2020) have examined the rotation of the secondary in a binary asteroid system by considering the influence of the secondary's rotation on the mutual orbit.

Nevertheless, some questions remain. Such as how different the two approaches are, and if the SOR model can capture dynamics of the system or essentially the SOC model should be considered. In this work, we present a comparative study between SOC and SOR by surfing the phase space of both models, and try to answer these questions.

© The Author(s), 2022. Published by Cambridge University Press on behalf of International Astronomical Union

https://doi.org/10.1017/S1743921321001344 Published online by Cambridge University Press

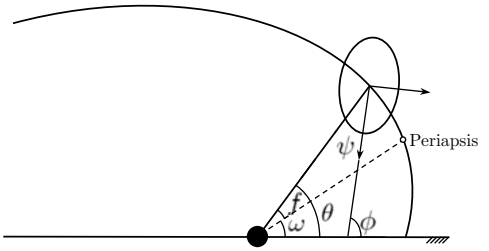

Figure 1. Geometry of spin-orbit coupling.

2. Equations of motion

Here, we provide a Hamiltonian of the SOC for the planar case. All the usual assumptions apply here as well. We utilize the gravitational potential energy function up to the fourth-order in terms of Stokes coefficients. We assume that an ellipsoidal asteroid of mass m_s is subjected to the gravitational attraction of a homogenous spherical asteroid with mass m_p, and the center of mass of the ellipsoid moves on a variable orbit, as we show in Figure 1. In the SOC, unlike the SOR, the mutual orbit varies. Therefore, the periapsis varies, and we need an appropriate reference, as depicted in Figure 1.

The gravitational potential energy for SOC model is as follows (Hou *et al.* (2017)):

$$V(r,\psi) = -Gm_pm_s\left\{\frac{1}{r}+\frac{1}{r^3}\left[-\frac{a_s^2C_{20}}{2}+\frac{a_s^2C_{22}}{4}\cos(2\psi)\right]\right.$$
$$\left.+\frac{1}{r^5}\left[\frac{3a_s^4C_{40}}{8}+\frac{a_s^4C_{42}}{24}\cos(2\psi)+\frac{a_s^4C_{44}}{192}\cos(4\psi)\right]\right\}$$

where G is the universal gravitational constant, C_{ij} are Stokes coefficients calculated as follows (Balmino, 1994):

$$C_{20} = \frac{1}{5a_s^2}\left(c_s^2-\frac{a_s^2+b_s^2}{2}\right) \quad C_{22} = \frac{1}{20a_s^2}\left(a_s^2-b_s^2\right)$$
$$C_{40} = \frac{15}{7}\left(C_{20}^2+2C_{22}^2\right) \quad C_{42} = \frac{5}{7}C_{20}C_{22} \quad C_{44} = \frac{5}{28}C_{22}^2$$

where a_s, b_s and c_s are the semi-axes of the secondary with $a_s \geq b_s \geq c_s$. Hence, the mass normalized Hamiltonian of the SOC model, including orbital and rotational kinetic energies, and the above gravitational potential energy,is given below:

$$H\left(t,r,\dot{r},\vartheta,\dot{\vartheta},\phi,\dot{\phi}\right) = \frac{1}{2}\left(\dot{r}^2+r^2\dot{\vartheta}^2\right)-\frac{\mu}{r}+\frac{I_3}{2m}\dot{\phi}^2-\mu\left\{-\frac{a_s^2C_{20}}{2r^3}+\frac{3a_s^4C_{40}}{8r^5}\right.$$
$$\left.+\left[\frac{a_s^2C_{22}}{4r^3}+\frac{a_s^4C_{42}}{24r^5}\right]\cos(2\phi-2\vartheta)+\frac{a_s^4C_{44}}{192r^5}\cos(4\phi-4\vartheta)\right\}$$

where I_3 is the moment of inertia, m is $\frac{m_pm_s}{m_p+m_s}$ and is called reduced mass, $\mu = G(m_p+m_s)$ and ϑ, measured from the reference, is the sum of true anomaly f and argument of periapsis ω. The first two terms describe the Keplerian motion, and the third term represents the free rotational motion. The last term is the asphericity perturbation resulting in the orbital and rotational alteration of the secondary asteroid motion. The Hamiltonian is a conserved quantity.

We define the unit of mass such that $m=1$, and take a_s as the unit of length. We also choose the unit of time such that $\mu=1$. Now, let us introduce the generalized coordinates and momentums $(r,p_r,\vartheta,p_\vartheta,\phi,p_\phi)$ where r , ϑ and ϕ are the generalized coordinates,

https://doi.org/10.1017/S1743921321001344 Published online by Cambridge University Press

as shown in Figure 1 and p_r, p_ϑ and p_ϕ are the conjugated generalized momentums. Therefore, we can write

$$H = \frac{1}{2}p_r^2 + \frac{p_\vartheta^2}{2r^2} + \frac{1}{2\bar{I}_3}p_\phi^2 + V\left(r, \phi - \vartheta\right)$$

where $\bar{I}_3$ is the mass normalized moment of inertia. We use an F_2-type generating function $F_2(\vartheta, \phi, p_\psi, p_\vartheta) = (\phi - \vartheta)\, p_\psi + \phi p_\vartheta$, for canonical transfer of the Hamiltonian (2) to

$$H\left(t, r, p_r, \psi, p_\psi, \vartheta, p_\vartheta\right) = \frac{p_r^2}{2} + \left(\frac{1}{2r^2} + \frac{1}{2\bar{I}_3}\right)p_\psi^2 + \frac{p_\vartheta^2}{2\bar{I}_3} + \frac{p_\psi p_\vartheta}{\bar{I}_3} + V\left(r, \psi\right)$$

Because the new generalized coordinate ϑ does not appear in the Hamiltonian, its conjugated generalized momentum p_ϑ is conserved. Finally, we can derive the equations of motion from the above Hamiltonian using the canonical formulation:

$$\dot{\vec{q}} = \frac{\partial H}{\partial \vec{p}} \quad \text{and} \quad \dot{\vec{p}} = -\frac{\partial H}{\partial \vec{q}} \tag{6}$$

3. Cartography of Resonances

In this section, we compare the phase space of the SOC and the SOR through cartography of resonances. To this end, we utilize the Fast Lyapunov Indicator (FLI) maps (Froeschlé *et al.* (1997)). For a regular motion, the value of FLI grows linearly, whereas, for a chaotic motion, the value of FLI increases exponentially. Hence, by computing FLI, we could distinguish between chaotic and regular motions. We report the FLI via a color scale, such that the highest FLI values are shown in brown, and the lowest values are shown in blue. We consider a set of 300x300 initial conditions placed on a regular grid in the plane $\left(\dot{\phi}/n, \phi\right)$, where normalized angular velocity ranges from 0 to 2.5, while the angle ϕ ranges from 0 to π. To produce the FLI maps, we find that the proper integration time is 100 times the non-dimensional orbital period. We choose different values of non-dimensional orbital semi-major axis, eccentricity, argument of latitude, mass ratio of bodies, and non-dimensional semi-axes of the secondary to generate a cartographic image of the phase space, and compare the resulting phase space for both models.

In the first case, we choose $a = 5,\ e = 0,\ f + \omega = 0,\ m_s/m_p = 0.75,\ \left(\bar{a}_s : \bar{b}_s : \bar{c}_s\right) = (1 : 0.95 : 0.90)$, and numerically integrate the equations, including equations of spin-orbit problems and their corresponding variational equations. As evident in Figure 2, for a circular orbit, the 1:1 resonance is the only resonance. The synchronous resonance plays a significant role in the dynamics of both models. However, there are some differences between the models. First, the maximum value of FLIs near separatrix of synchronous resonance is 20 for the SOC and 7 for the SOR. That means, near separatrix, spin of the secondary in the SOC model could be more chaotic than the SOR model. Second, an invariant torus with high FLI values presents near 2:3 resonance in the SOC (Figure 2).

We consider an eccentric orbit with $a = 10,\ e = 0.01,\ f + \omega = \pi/4,\ m_s/m_p = 0.25,\ \left(\bar{a}_s : \bar{b}_s : \bar{c}_s\right) = (1 : 0.90 : 0.45)$ as the second case. As can be seen from Figure 3, the values of FLIs are in the same order. According to the value of the argument of latitude, we expect that stable and unstable configurations of both systems are at $\phi = \pi/4,\ 5\pi/4$ respectively, as demonstrated in Figure 3. In both models, the homoclinic intersection of stable and unstable manifolds results in a chaotic layer around the synchronous resonance, where the onset of chaos is. Nevertheless, in the SOR model, there is a chain of three islands around the synchronous resonance. Also, the separatrix of 2:3 resonance is visible in this model. It seems that in the SOR model, more initial grids have high FLIs values. In the SOC model, there are no secondary islands and the chaotic layer around the synchronous resonance is narrower than the other model. Instead of the 2:3 resonance island, we see a chaotic layer.

https://doi.org/10.1017/S1743921321001344 Published online by Cambridge University Press

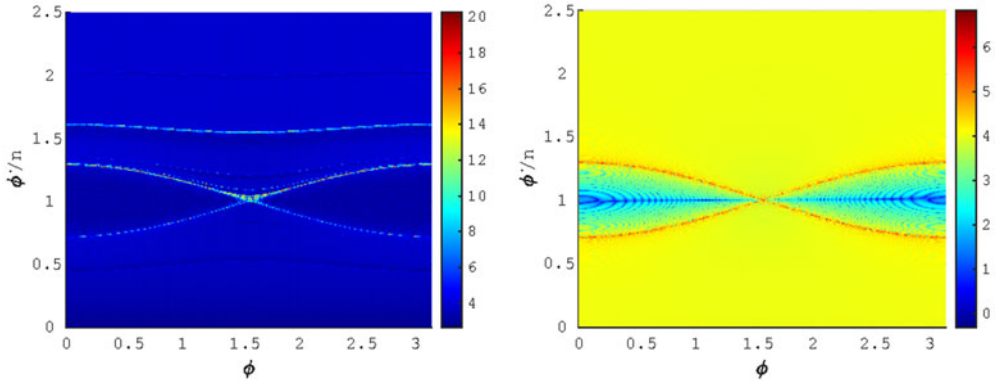

Figure 2. FLI maps for spin-orbit coupling (left) and spin-orbit resonance (right). The Initial values are $a = 5$, $e = 0$, $f + \omega = 0$, $m_s/m_p = 0.75$, $(\bar{a}_s : \bar{b}_s : \bar{c}_s) = (1 : 0.95 : 0.90)$.

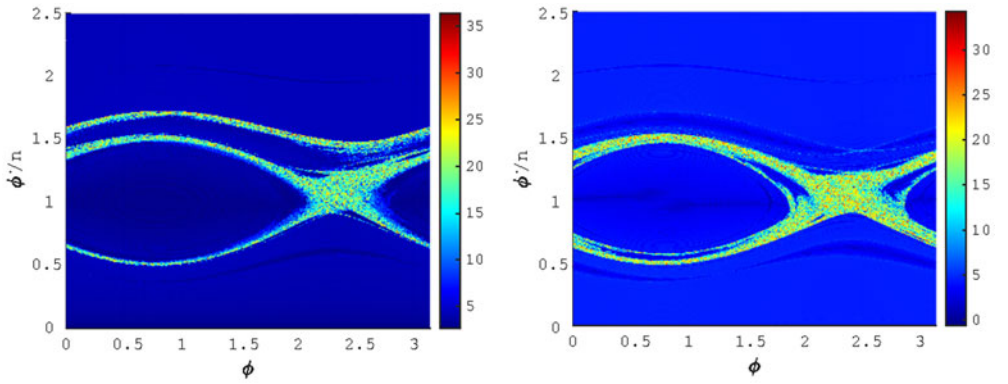

Figure 3. FLI maps for spin-orbit coupling (left) and spin-orbit resonance (right). The Initial values are $a = 10$, $e = 0.01$, $f + \omega = \pi/4$, $m_s/m_p = 0.25$, $(\bar{a}_s : \bar{b}_s : \bar{c}_s) = (1 : 0.90 : 0.45)$.

We calculate the FLI map for $a = 15$, $e = 0.05$, $f + \omega = \pi/2$, $m_s/m_p = 0.10$, $(\bar{a}_s : \bar{b}_s : \bar{c}_s) = (1 : 0.80 : 0.60)$. Figure 4 shows the resulting FLI maps. The eccentric orbit of the secondary causes the appearance of other resonances, of which some are overlapping. However, the synchronous resonance has sizeable resonant islands and still prevails in the phase space. The overlapping of nearby resonances with the synchronous resonance leads to a thick chaotic layer around it. The 3:1 secondary resonance exists in both models, although its separatrix begins to be destroyed. In Figure 4, it is quite obvious that in the SOR model compared with the SOC model, more initial grids have high FLIs values. Three persistence islands in the thick chaotic layer in the SOC model versus four islands in the SOR model is another difference. Also, in the left panel of Figure 4, the 7:4 resonance is evident.

If we consider $a = 20$, $e = 0.15$, $f + \omega = \pi$, $m_s/m_p = 0.05$, $(\bar{a}_s : \bar{b}_s : \bar{c}_s) = (1 : 0.70 : 0.35)$ we can see the resulting maps are dramatically different, as indicated in Figure 5. While the islands of 2:1 and 2:3 resonances are persevering for the SOC model, the rotation of the secondary is chaotic for the normalized rotation rate of 2 in the SOR model.

Now we take $a = 50$, $e = 0.25$, $f + \omega = 5\pi/4$, $m_s/m_p = 0.01$, $(\bar{a}_s : \bar{b}_s : \bar{c}_s) = (1 : 0.50 : 0.50)$ and generate FLI maps (see Figure 6). In this case, although the phase space portraits are dissimilar, we face widespread chaos in both models. We can see a considerable regular region for the rotation of the secondary with a low normalized

https://doi.org/10.1017/S1743921321001344 Published online by Cambridge University Press

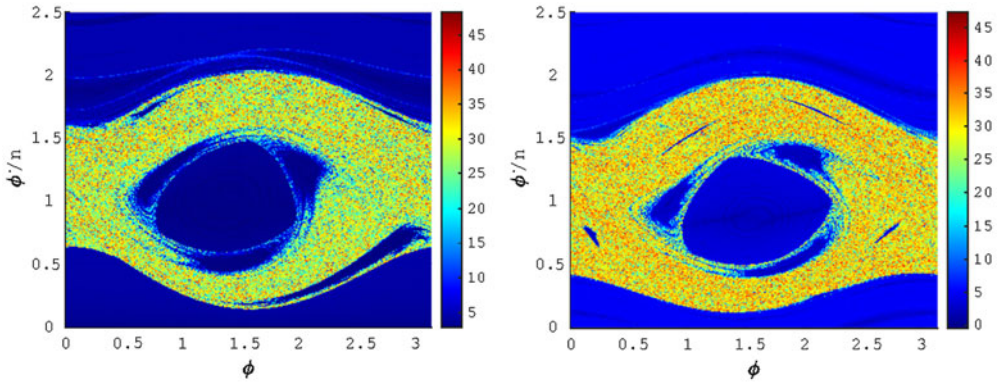

Figure 4. FLI maps for spin-orbit coupling (left) and spin-orbit resonance (right). The Initial values are $a = 15$, $e = 0.05$, $f + \omega = \pi/2$, $m_s/m_p = 0.10$, $(\bar{a}_s : \bar{b}_s : \bar{c}_s) = (1 : 0.80 : 0.60)$.

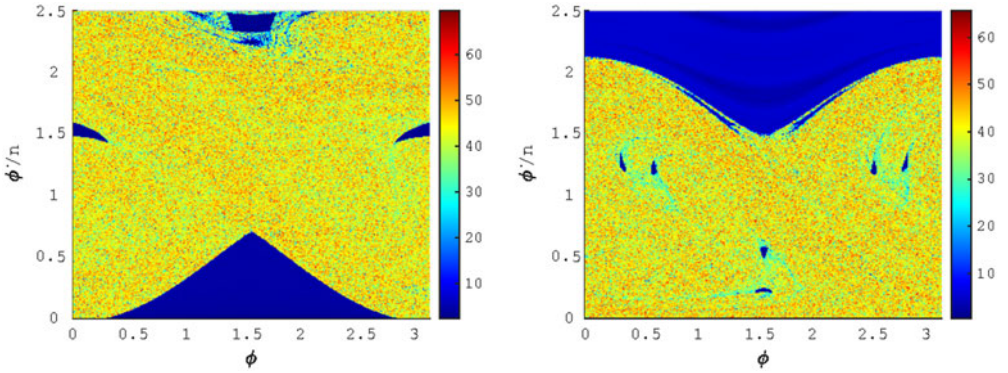

Figure 5. FLI maps for spin-orbit coupling (left) and spin-orbit resonance (right). The Initial values are $a = 20$, $e = 0.15$, $f + \omega = \pi$, $m_s/m_p = 0.05$, $(\bar{a}_s : \bar{b}_s : \bar{c}_s) = (1 : 0.70 : 0.35)$.

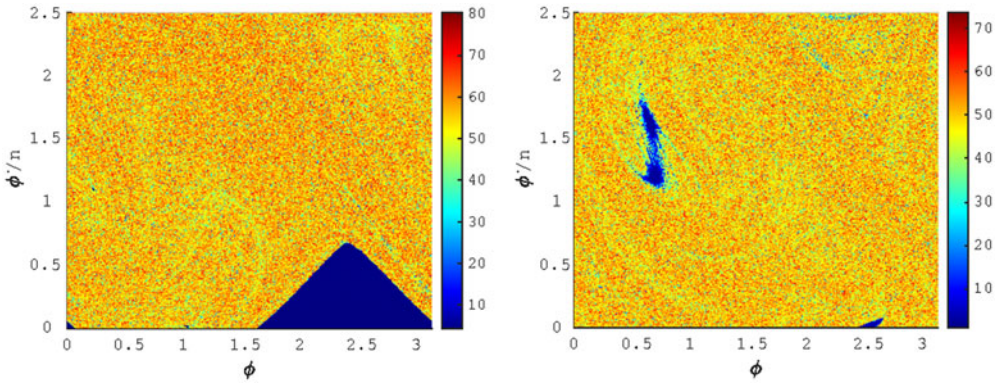

Figure 6. FLI maps for spin-orbit coupling (left) and spin-orbit resonance (right). The Initial values are $a = 50$, $e = 0.25$, $f + \omega = 5\pi/4$, $m_s/m_p = 0.01$, $(\bar{a}_s : \bar{b}_s : \bar{c}_s) = (1 : 0.50 : 0.50)$.

rotation rate in the SOC model. Comparingly, a tiny island, in the vicinity of 2:3 resonance, surrounded by the chaotic sea, is noticeable in the SOR model.

Since it may be inferred that the large chaotic region in Figure 6 is because of the high asphericity of the secondary, we consider the previous case with a different semi-axis, i.e., $(\bar{a}_s : \bar{b}_s : \bar{c}_s) = (1 : 0.90 : 0.90)$. It is evident that the phase space is occupied with a large

https://doi.org/10.1017/S1743921321001344 Published online by Cambridge University Press

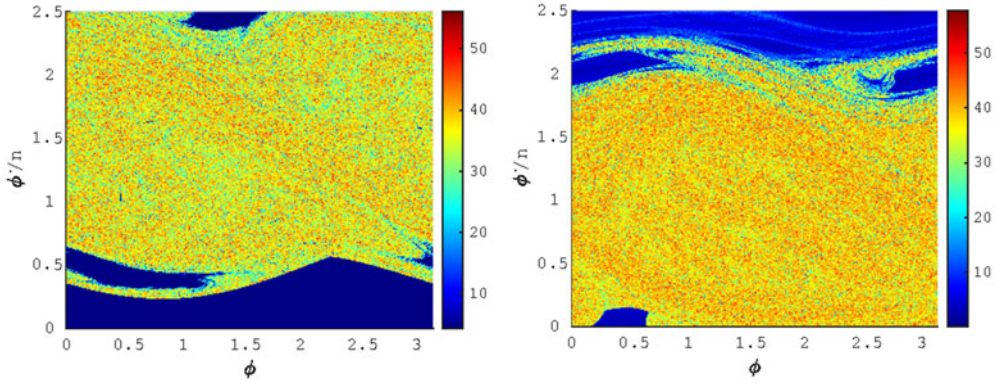

Figure 7. FLI maps for spin-orbit coupling (left) and spin-orbit resonance (right). The Initial values are $a = 50$, $e = 0.25$, $f + \omega = 5\pi/4$, $m_s/m_p = 0.01$, $(\bar{a}_s : \bar{b}_s : \bar{c}_s) = (1 : 0.90 : 0.90)$.

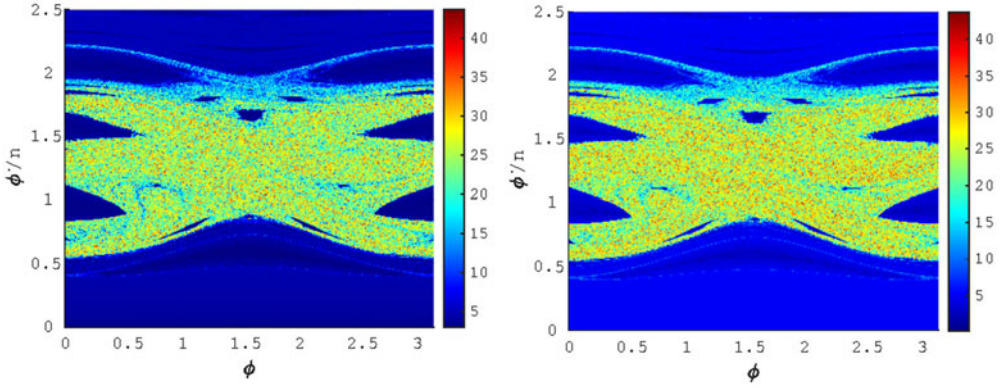

Figure 8. FLI maps for spin-orbit coupling (left) and spin-orbit resonance (right). The Initial values are $a = 20$, $e = 0.15$, $f + \omega = 0$, $m_s/m_p = 0.01$, $(\bar{a}_s : \bar{b}_s : \bar{c}_s) = (1 : 0.95 : 0.90)$.

chaotic region (Figure 7). However, there is a major difference between the two models. While the 2:1 resonance island exists in the phase space of the SOC model, and rotation of the secondary for a low normalized rotation rate is regular, the 1:2 resonances region is preserved in the phase space of the SOR model. In addition, the high normalized rotation rate of the secondary is regular in the SOR model.

There may be some systems where using both models have the same phase space portrait. For instance, we consider a system with $a = 20$, $e = 0.15$, $f + \omega = 0$, $m_s/m_p = 0.01$, $(\bar{a}_s : \bar{b}_s : \bar{c}_s) = (1 : 0.95 : 0.90)$. The FLI maps are depicted in Figure 8. There is no difference between them, though more initial grids still have high FLIs values in the SOR model.

4. Conclusion

We explore the phase space of spin-orbit problem in both models of SOC and SOR. The comparison of phase space structures shows noticeable differences in the models. That is to say, the SOR model cannot correctly capture the dynamics of the system, and the SOC model is more appropriate. However, this depends on the orbital and physical properties of the system. Because there may be some systems that show same results in both models, the question of which model is suitable should be examined in each case.

https://doi.org/10.1017/S1743921321001344 Published online by Cambridge University Press

References

Celletti, Alessandra and Chierchia, Luigi 2000, *Celestial Mechanics and Dynamical Astronomy*, 76, 229

Froeschlé, Claude and Lega, Elena and Gonczi, Robert 1997, *Celestial Mechanics and Dynamical Astronomy*, 67, 41

Goldreich, Peter and Peale, Stanton 1966, *AJ*, 71, 425

Hou, Xiyun and Xin, Xiaosheng 2017, *AJ*, 154, 257

Hou, Xiyun and Scheeres, Daniel J and Xin, Xiaosheng 2017, *Celestial Mechanics and Dynamical Astronomy*, 127, 369

Misquero, Mauricio and Ortega, Rafael 2020, *SIAM Journal on Applied Dynamical Systems*, 19, 2233

Nadoushan, Mahdi Jafari and Assadian, Nima 2016, *Nonlinear Dynamics*, 85, 1837

Naidu, Shantanu P and Margot, Jean-Luc 2015, *AJ*, 149, 80

Wang, HS and Hou, XY 2020, *MNRAS*, 493, 171

Wisdom, Jack and Peale, Stanton J and Mignard, François 1984, *Icarus*, 58, 137

https://doi.org/10.1017/S1743921321001344 Published online by Cambridge University Press